Journal of Magnetic Resonance 210 (2011) 238–245

Contents lists available at ScienceDirect

Journal of Magnetic Resonance

journal homepage: www.elsevier.com/locate/jmr

Analysis of remote detection travel time curves measured from microfluidic channels

Ville-Veikko Telkki [a,*], Vladimir V. Zhivonitko [b]

[a] NMR Research Group, Department of Physics, University of Oulu, P.O. Box 3000, FIN-90014, Finland
[b] International Tomography Center, 3A Institutskaya Street, Novosibirsk 630090, Russia

ARTICLE INFO

Article history:
Received 13 January 2011
Revised 11 March 2011
Available online 17 March 2011

Keywords:
Remote detection NMR
Travel time
Microfluidics
Poiseuille flow
Plug flow

ABSTRACT

Remote detection technique can increase sensitivity of an NMR experiment by several orders of magnitude in microfluidic applications. Travel time experiment is a basic remote detection NMR experiment, which reveals the travel time distribution of the molecules flowing from the encoding coil region to the detector. In this article, we focus on analyzing how flow type (Poiseuille or plug flow), diffusion, dispersion and geometry of the flow channels are manifested in the travel time curves measured from microfluidic channels. We demonstrate that remote detection travel time experiment could be used even as an alternative NMR method for measuring self-diffusion coefficient of a fluid without magnetic field gradients. In addition, we introduce a modified travel time pulse sequence, which removes the signal of unencoded fluid spins as well as the background signal arising from the material inside or close to the detector.

1. Introduction

Microfluidics deals with the control and manipulation of fluids in channels with dimensions below one millimeter [1]. Small dimensions enable, for instance, efficient heat exchange and precise control of chemical reactions, and therefore microfluidics offer substantial promises for future technologies. Applications of microfluidic systems are already diverse ranging from the analysis of DNA and proteins to examination and manipulation of samples containing a single cell [2–4].

In principle, NMR is an optimal method for investigating microfluidic flow behavior, because it provides versatile spatial, dynamic and spectroscopic information, it does not require addition of markers, and the devices under investigation do not need to be transparent [5,6]. However, typically the dimensions of the fluid channels in a microfluidic device are several orders of magnitude smaller than the dimensions of the whole device, and hence the sensitivity of an NMR experiment performed with a large coil around the device is very poor because of low filling factor and low sensitivity of the large coil. The sensitivity can be increased by fabricating planar microcoils directly on the microfluidic device [7–9] or using a large surface coil set on top of a planar microfluidic device [10]. Contrary to the previous techniques, remote detection (RD) NMR enables investigating the whole microfluidic device volume with optimized detection sensitivity.

In RD NMR, the information about a sample is encoded in the spin coherences of a probe fluid, and thereafter the probe fluid is transported to a different location outside the sample for observing the NMR signal [11]. Usually, the encoding is carried out by a large coil around the sample, and the detection is performed by another, smaller and more sensitive coil with optimized filling factor. In some cases, especially in low field applications, alternative detection methods such as atomic magnetometry are used [12–14]. RD NMR provides also time-of-flight (TOF) information as the probe molecules encoded in different parts of the sample arrive in the detector at different times. The encoding may cover spectroscopic, spatial or dynamic information. If the encoding step corresponds to the phase encoding in a conventional MRI experiment, it is possible to obtain 3D TOF images about the fluid flow that reveal the flow paths and dispersion of fluid molecules [15]. RD NMR has been used to characterize porous media [11,16,17], rocks [15], membranes [18], microfluidic devices [19–23] and wood [24], and it has also been applied in monitoring spin coherence transfer in chemical transformations [25], relaxation measurements [26] and gas extraction applications [27].

In the RD NMR experiments presented in this article, the encoding of spin coherences is performed with a large birdcage coil around a microfluidic device, and detection is carried out by a small solenoid coil, whose sensitivity is 600 times better than that of the encoding coil [23]. The sensitivity boost given by RD technique is enough for measuring signal from thermally polarized water but not enough for observing signal from thermally polarized propane gas, whose molecular number density is three orders

* Corresponding author. Fax: +358 8 5531287.
E-mail address: ville-veikko.telkki@oulu.fi (V.-V. Telkki).

1090-7807/$ - see front matter © 2011 Elsevier Inc. All rights reserved.
doi:10.1016/j.jmr.2011.03.011

of magnitude smaller than that of water. Additional sensitivity boost (80-fold as compared with thermally polarized gas), that enables performing the gas phase experiments, is obtained by utilizing the parahydrogen-induced polarization (PHIP) technique [28,29] based on heterogeneous hydrogenation reaction [23,30–33].

Typically, one of the first steps in RD NMR investigations is to determine the travel time distribution of the probe molecules flowing from the encoding coil region to the detector. In the original travel time experiment [11], the magnetization of the probe fluid inside the encoding coil is first inverted by a π-pulse and then the arrival of the encoded molecules in the detector is observed applying a train of $\pi/2$-pulses (Fig. 2a). The decrease in the amplitude of the observed signal indicates when the inverted spins arrive in the detector, and therefore the measured signal as a function of the travel time (travel time curve) reveals the travel time distribution. Here, we present travel time curves measured from several microfluidic systems and analyze what kind of information about the flow type, diffusion, dispersion and geometry of the flow channels they contain. In addition, we introduce an alternative, modified travel time pulse sequence, which removes the signal of unencoded probe fluid spins as well as the background signal arising from the solid material inside or close to the detector.

2. Theoretical analysis

2.1. Definition of travel time distribution

Consider one-dimensional flow of the probe fluid in the x direction. Assume that the detector is a point-like object at x', and t is the time taken by a probe fluid molecule to travel from the encoding coil region to the detector. The travel time distribution can be defined to be the total probability, $\Psi(x', t)$, of finding an encoded spin at position x' at time t, which can be represented as [5]

$$\Psi(x', t) = \int \Psi(x, 0) P(x|x', t) dx \tag{1}$$

Here, $\Psi(x, 0)$ is in fact the concentration of the encoded spins right after the encoding, and it is zero outside the encoding coil region. We assume that $\Psi(x, 0)$ is normalized so that the total concentration including both encoded and unencoded spins at the detector ($x = x'$) is one. $P(x|x', t)$ is the propagator, *i.e.*, the probability that the position of a molecule is x at time t if it was x' at zero time.

In the general case, when dealing with three dimensional flow and not a point-like detector, variables x and x' are replaced by vectors $\mathbf{r}$ and $\mathbf{r}'$ in the travel time distribution function, and the function contains also integration of $\mathbf{r}'$ variable over the detection region:

$$\Psi(t) = \int \int \Psi(\mathbf{r}, 0) P(\mathbf{r}|\mathbf{r}', t) d\mathbf{r} d\mathbf{r}' \tag{2}$$

Like above, we assume that $\Psi(\mathbf{r}, 0)$ is normalized so that the integral of the total concentration including both encoded and unencoded spins over the detector volume is one.

2.2. Travel time distribution of a fluid flowing in a capillary

Consider a simple RD experiment, in which the probe fluid is flowing into positive x direction in a cylindrical capillary. An encoding coil is around the capillary and a point-like detector is at a certain distance away from the encoding coil as shown in Fig. 1a. In the case of Poiseuille flow, the velocity of the molecules as a function of the transverse distance r from the axis of the tubing can be expressed by the Hagen–Poiseuille equation

$$v_l = v_{l\max}\left[1 - \left(\frac{r}{R}\right)^2\right], \tag{3}$$

where $v_{l\max}$ is the maximum velocity and R is the radius of the capillary. Therefore, one-dimensional propagator for the Poiseuille flow, if self-diffusion is not taken into account, is [34,35]

$$P_l(x|x', t) = \begin{cases} \frac{1}{v_{l\max} t}, & \text{when } x \leqslant x' \leqslant x + v_{l\max} t \\ 0, & \text{elsewhere} \end{cases}, \tag{4}$$

i.e., the propagator a top-hat shape between x and $x + v_{l\max}t$. In the case of plug flow, all the molecules have the same velocity v_p, and hence the propagator is

$$P_p(x|x', t) = \delta(x' - x - v_p t), \tag{5}$$

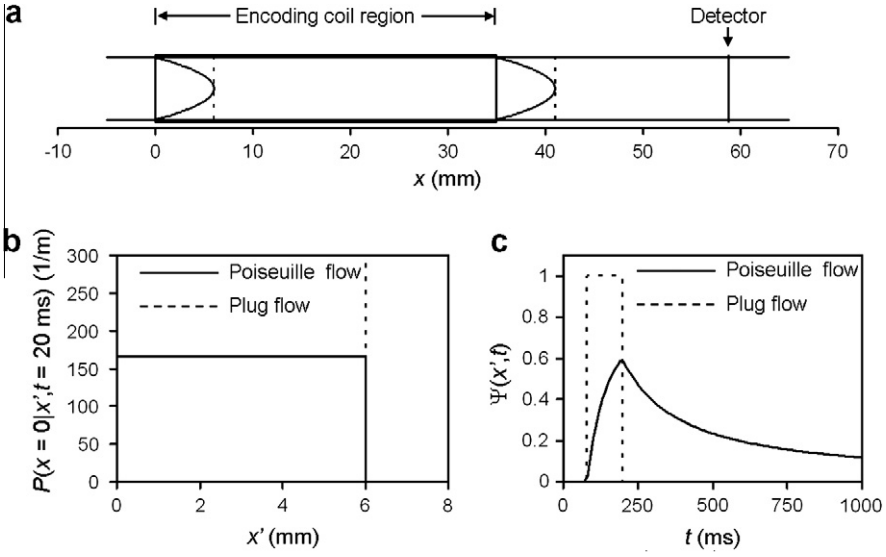

Fig. 1. Poiseuille and plug flow in a cylindrical tubing. (a) A model system used in the calculations. The encoding coil region is $0 \leqslant x \leqslant 35$ mm and the point-like detector is at $x = 58.8$ mm. Velocities $v_{l\max}$ and v_p were set to be 300 mm/s. Parabolic solid lines (Poiseuille flow) and straight dashed lines (plug flow) show the positions of molecules initially at the left ($x = 0$ mm) and right ($x = 35$ mm) edge of the encoding coil 20 ms after the encoding. (b) Propagators for the molecules initially at $x = 0$ at $t = 20$ ms calculated by Eqs. (4) and (5). (c) Travel time distributions calculated by substituting Eqs. (4) and (5) to Eq. (1).

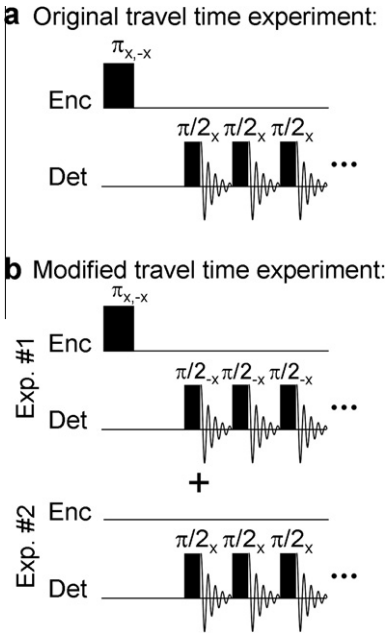

Fig. 2. Pulse sequence of the original travel time experiment (a) and modified travel time experiment (b). In the modified travel time experiment, two different experiments are carried out, from which one contains a π inversion pulse and another does not, and the signals of the experiments are summed together.

where $\delta(x)$ is the Dirac delta function. The Poiseuille and plug flow propagators are illustrated in Fig. 1b. The travel time distributions for Poiseuille and plug flow calculated by substituting Eqs. (4) and (5) into Eq. (1) are shown in Fig. 1c. Poiseuille flow travel time distribution is broad as the molecules in the center of the tubing arrive rapidly in the detector whereas the travel time of the molecules close to the surface is very long. The distribution has nonzero value above $t = (x' - \Delta x)/v_{lmax}$, which is the time instance when the fastest encoded spins at $x = \Delta x$ during encoding arrive to the detector (Δx is the length of the encoding coil region). The value of $\Psi(x', t)$ is always smaller than one because there are always both encoded and unencoded spins in the detector. The distribution has its maximum value at $t = x'/v_{lmax}$, physically corresponding to the time instant when the first unencoded spins at $x < 0$ during encoding arrive in the detector. The plug flow distribution is a top-hat function. The time instances corresponding to the left and right edge of the distribution are $t = (x' - \Delta x)/v_p$ and $t = x'/v_p$, respectively. Within this time region, the amplitude of the distribution is one because the detector contains only encoded spins.

As the length of the detector used in the experiments is finite (3 mm), the analysis of the travel time distribution should include integration over detection region as shown in Eq. (2). However, the travel time distributions resulted from the Monte Carlo simulations (not shown) taking into account the finite detection volume are in excellent agreement with the distributions calculated by Eq. (1), showing that the point-like detector approximation is very precise in the case of the current experimental setup, and therefore Eq. (1) is used in the analysis instead of Eq. (2).

2.3. Original and modified travel time experiment

In the original travel time experiment, the magnetization in the encoding coil region is inverted by a π-pulse, and then the amplitude of the magnetization in the detector is monitored by a train of $\pi/2$-pulses as shown in Fig. 2a. The encoded (inverted) spins give negative contribution to the signal, which is proportional to $-\Psi(x', t)$, whereas the unencoded spins give positive contribution, which is proportional to $1 - \Psi(x', t)$. Therefore, the normalized observed amplitude in the original travel time experiment, $A_o(t)$, is

$$A_o(t) = -\Psi(x', t) + [1 - \Psi(x', t)] = 1 - 2\Psi(x', t), \tag{6}$$

from which one can resolve the travel time distribution function:

$$\Psi(x', t) = \frac{1}{2}[1 - A_o(t)]. \tag{7}$$

Modified travel time experiment comprises two different experiments whose signals are added together as shown in Fig. 2b. Experiment #1 contains a π inversion pulse. As the phase of the detector $\pi/2$-pulses is $-x$, the encoded (inverted) spins give now positive contribution to the signal (the detector phase is assumed to be x), which is proportional to $\Psi(x', t)$, whereas the unencoded spins give negative contribution, which is proportional to $-[1 - \Psi(x', t)]$. Experiment #2 does not contain the inversion pulse. As the phase of the detector $\pi/2$ pulses is now x, all the spins give positive contribution to the signal, and the normalized observed amplitude is time independent, and its value is 1. Hence, when the signals of experiments #1 and #2 are summed together, the contribution of the unencoded spins disappear, and the normalized observed amplitude is

$$A_m(t) = \Psi(x', t). \tag{8}$$

Eq. (8) shows that the observed amplitude function in the modified travel time experiment is directly the travel time distribution function, *i.e.*, no such inversion of the travel time curve as in the case of the original travel time experiment is needed for resolving the travel time distribution function. In addition, the signal arising from the non-flowing spins inside or close to the detector is removed. The phase cycling in the original and modified experiment shown in Fig. 2 removes also residual transverse magnetization induces by imperfect inversion pulse.

2.4. Effect of imperfect inversion pulse on travel time distribution

Next we consider the effect of imperfect inversion pulse on the observed amplitude. Assume that the rotation angle caused by the inversion pulse is $(\pi-\alpha)$ instead of π. In this case, the magnitude of longitudinal magnetization after the inversion pulse is decreased by the factor of $\cos(\alpha)$ as compared with the case when the inversion pulse is perfect. In the original travel time experiment, the observed amplitude is now

$$\begin{aligned} A_o(\alpha, t) &= -\cos(\alpha)\Psi(x', t) + [1 - \Psi(x', t)] \\ &= 1 - 2\cos^2\left(\frac{\alpha}{2}\right)\Psi(x', t), \end{aligned} \tag{9}$$

and hence the observed travel time distribution calculated according to Eq. (7) is

$$\Psi_{obs}(x', t) = \frac{1}{2}[1 - A_o(\alpha, t)] = \cos^2\left(\frac{\alpha}{2}\right)\Psi(x', t). \tag{10}$$

In the modified travel time experiment, the signal amplitude of the spins initially in the encoding region is proportional to $\cos(\alpha)\Psi(x', t)$ and $\Psi(x', t)$ in the experiment #1 and #2, respectively, and the observed amplitude is

$$\begin{aligned} A_m(\alpha, t) &= \frac{1}{2}[1 + \cos(\alpha)]\Psi(x', t) = \cos^2\left(\frac{\alpha}{2}\right)\Psi(x', t) \\ &\equiv \Psi_{obs}(x', t). \end{aligned} \tag{11}$$

Hence, according to Eqs. (10) and (11), imperfect inversion scales the travel time distribution by factor of $\cos^2(\alpha/2)$ both in the original and modified travel time experiment.

2.5. Normalization of the measured amplitude

Eq. (7) requires that the observed amplitude, A_o, in the original travel time experiment is normalized so that when the detection coil contains only non-inverted spins, $A_o = 1$. In practice, the normalization can be realized by dividing the measured travel time curve amplitudes by the amplitude of the signal of the corresponding experiment that does not contain the inversion pulse or by the amplitude of the signal measured before inverted spins have arrived in the detector or after they have left the detector. The normalization in the experiments shown below is performed according to the last option.

Eq. (8), in turn, requires that the observed amplitude, A_m, in the modified travel time experiment is normalized so that when the detection coil contains only encoded spins, $A_m = 1$. Because of dispersion, typically there are always both encoded and unencoded spins inside the detection coil, and therefore there is no direct way to do the normalization. However, the normalization can be performed indirectly by dividing the measured travel time curve amplitudes by the amplitude of the signal of the corresponding experiment in which experiment #2 in Fig. 2b is performed two times and the observed signals are added together. The background signal arising form stationary material is removed from the spectra of the direct travel time experiment but not from the normalization experiment, and this fact has to be taken into account in the normalization. In the experiment shown below, we did not perform this kind of normalization; instead, we simply normalized the maximum amplitude to be 1.

2.6. Effect of T_1 relaxation on travel time distribution

The effect of spin–lattice (T_1) relaxation on the observed travel time distribution varies depending on whether the fluid contains thermally polarized or hyperpolarized spins.

First, we assume that the spins are *thermally polarized*, and they are in thermal equilibrium at the beginning of the experiment. Furthermore, we assume that the strength of the external magnetic field felt by the spins is constant during the experiment. After the inversion pulse, the magnetization vector of the inverted spins begins to evolve toward thermal equilibrium due to T_1 relaxation, and therefore the observed amplitude of the encoded spins is proportional to $[1 - 2\exp(-t/T_1)]\Psi(x', t)$. The magnetization vector of the unencoded spins stay in the thermal equilibrium, and the observed amplitude is proportional to $1 - \Psi(x', t)$. Hence, the overall observed normalized amplitude is

$$A_o(t) = [1 - 2\exp(-t/T_1)]\Psi(x', t) + 1 - \Psi(x', t) = 1 - 2\exp(-t/T_1)\Psi(x', t). \quad (12)$$

The observed travel time distribution calculated according to Eq. (7) is

$$\Psi_{obs}(x', t) = \frac{1}{2}[1 - A_o(\alpha, t)] = \exp(-t/T_1)\Psi(x', t), \quad (13)$$

i.e., the travel time distribution is weighted by the exponential factor $\exp(-t/T_1)$. It is straightforward to show that the observed normalized amplitude in the modified experiment is

$$A_m(t) = \exp(-t/T_1)\Psi(x', t), \quad (14)$$

i.e., also in this case the observed travel time distribution is weighted by the same exponential factor.

Next, we assume that the spins are *hyperpolarized* and the initial magnetization per unit volume right after the hyperpolarizing, M_0, is much larger than the thermal equilibrium magnetization, M_{eq}: $M_0 \gg M_{eq}$. After the hyperpolarizing, the magnetization begins to decay toward the thermal equilibrium value, which can be approximated to be zero, because M_{eq} is negligible as compared with M_0. If T_{pd} is the mean travel time from the polarizer to the detector, the magnetization of the unencoded spins in the detector is $M_1 = \exp(-T_{pd}/T_1)M_0$. The inversion pulse is applied for time t before the detection. Just before the inversion pulse the average magnetization is $M_2 = \exp[-(T_{pd} - t)/T_1]M_0$. After the inversion, the magnetization evolves toward the thermal equilibrium value $M_{eq} \approx 0$, and therefore the magnetization of the encoded spins at time t after the inversion is $-M_2\exp(-t/T_1) = -\exp(-T_{pd}/T_1)M_0 = -M_1$. Hence, the observed normalized amplitude is

$$A_o(t) = -\Psi(x', t) + 1 - \Psi(x', t) = 1 - 2\Psi(x', t). \quad (15)$$

The observed travel time distribution calculated according to Eq. (7) is

$$\Psi_{obs}(x', t) = \frac{1}{2}[1 - A_o(\alpha, t)] = \frac{1}{2}[1 - 1 + 2\Psi(x', t)] = \Psi(x', t), \quad (16)$$

i.e., T_1 relaxation does not change the shape of the travel time distribution. It can be shown that the observed normalized amplitude in the modified experiment is

$$A_m(t) = \Psi(x', t). \quad (17)$$

Therefore we can conclude that the observed travel time distribution is weighted by the factor $\exp(-t/T_1)$, when thermally polarized spins are used in the experiment, but T_1 relaxation does not change the shape of the distribution in the case of hyperpolarized spins.

3. Results and discussion

3.1. Plug-like flow in a capillary

In the first experiment, a mixture of hyperpolarized propane (16%), propene (11%) and hydrogen (73%) gas flowed in a capillary, which was set to lead through the encoding coil and the detection coil (see Fig. 3). The encoding coil height, distance between the

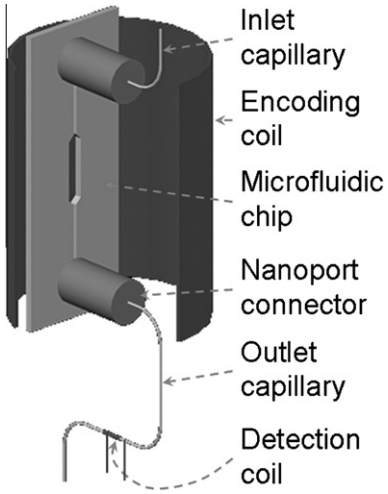

Fig. 3. Experimental setup. Two first experiments described in the text did not include the microfluidic chip, but, instead, the capillary led straightly through the encoding coil region. ID and OD of the capillary are 150 and 365 μm, respectively. The height and ID of the encoding coil are 35 and 25 mm, respectively. The detection coil was made of 120 μm diameter copper wire, which was wound around the outlet capillary. The length and ID of the coil were 3 mm and 365 μm, respectively. The experiments were performed on a Bruker DSX300 spectrometer, operating at a proton resonance frequency of 300 MHz and equipped with microimaging accessories. The encoding was carried out with a Bruker Micro 2.5 imaging probe and the detection with a home-build detection probe. Other experimental details are explained elsewhere [23].

encoding and detection coils and flow velocity were approximately the same as in the model system shown in Fig. 1a. Proton spin polarization of propane was increased by PHIP technique along with the experimental scheme termed ALTADENA [36]. The scheme produces two large signals in the spectrum with opposite phase arising from a polarized proton in CH_2 and CH_3 groups of propane as well as much weaker signals from other, thermally polarized protons. In practice, the latter signals were not observable. The details of the polarization procedure are described elsewhere [23].

The travel time curve measured using the original pulse sequence is shown in Fig. 4a. The amplitude of the signal begins to decrease at $t \sim 50$ ms, when the first inverted spins arrive in the detector. The curve reaches its minimum value at $t \sim 100$ ms. The minimum value is slightly above -1 most likely because of imperfect inversion pulse (the effect described by Eq. (9)). Notice that, since we are dealing with hyperpolarized fluid, T_1 relaxation does not increase the minimum amplitude of the curve (see Section 2.6). The travel time distribution calculated by Eq. (7) has been plotted in Fig. 4b. The maximum of the distribution was scaled to be one in order to eliminate the effect of imperfect inversion pulse. The shape of the distribution is characteristic of plug-like flow (compare with Fig. 1c). The Reynolds number of the gas was estimated to be very small (about 0.7), indicating laminar flow. However, as a typical diffusion coefficient D of a gas at room temperature is on the order of 10^{-5} m^2/s [37], the average diffusion time of propane across the 150 μm capillary can be estimated to be about 1 ms, which is much shorter than the travel time between encoding and detection coils (on the order of 100 ms). Hence, fast diffusion causes complete mixing of different flow lamellas, and plug flow profile is observed instead of Poiseuille flow.

The travel time distribution is not perfectly rectangular because of several factors, from which the most important are the axial diffusion of the gas and imperfect, non-rectangular excitation profile of the encoding coil. Because of the axial diffusion, the gas flow propagator is not anymore the Dirac delta function shown in Eq. (5), but it is [5]

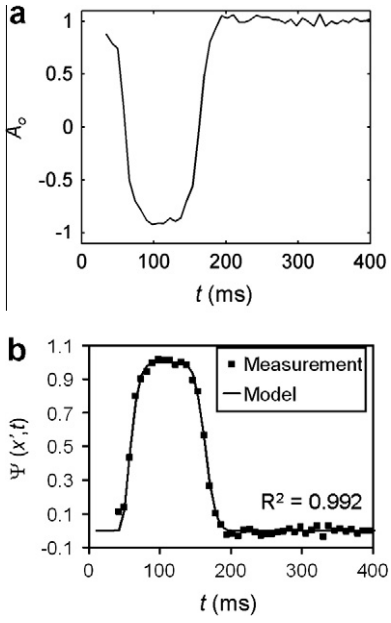

Fig. 4. (a) Travel time curve of hyperpolarized propane flowing in the capillary measured using the original travel time pulse sequence. Time resolution (time between successive detection coil $\pi/2$-pulses) in the experiment was 8 ms. Number of consecutive FID signals collected during one scan was 50. (b) Travel time distribution calculated by Eq. (7) and the model function fitted to the measured data points.

$$P(x|x',t) = \frac{1}{\sqrt{4\pi Dt}} \exp\left[\frac{-(x'-x-v_p t)^2}{4Dt}\right]. \quad (18)$$

Notice that the Taylor dispersion increases the effective diffusion coefficient value by $v_p^2R^2/48D$ in the long diffusion time limit [38].

For determining the excitation profile of the encoding coil, 1D spin-echo magnetic resonance image of a uniform water sample were measured along the flow direction. The flip angle of the excitation pulse depends on the strength of the transverse rf-field, $B_{rf}(x)$, and consequently the magnitude of the transverse magnetization after the pulse is proportional to $\sin[FB_{rf}(x)]$, where F is a constant. On the other hand, according to the principle of reciprocity [39], the detection sensitivity is also directly proportional to $B_{rf}(x)$, and therefore the image amplitude, $A(x)$, in the 1D water MRI experiment can be written as

$$A(x) = CB_{rf}(x)\sin[FB_{rf}(x)], \quad (19)$$

where C is a constant. The transverse rf-field profile of the encoding coil, $B_{rf}(x)$, was determined by the iterative fitting of Eq. (19) to the measured image amplitudes. The flip angle of the inversion pulse in the travel time experiment was assumed to be $2FB_{rf}(x)$. In order to calculate the theoretical travel time distribution, which takes into account both axial diffusion and imperfect excitation profile, Eq. (18) was substituted into Eq. (1) and $\Psi(x,0)$ was assumed to be $\cos^2[\alpha(x)/2]$, which is a factor arising from Eq. (10). Theoretical distribution was fitted to the experimental data points by letting parameters v_p, x' and D to vary. Notice that change in v_p changes only the position of the travel time distribution, whereas change in x' changes both the position and the width of the distribution. Change in D, in turn, changes only the shape of the distribution, and therefore all the before mentioned parameters can be fitted at the same time. The fit of the model curve to the experimental data points is excellent (see Fig. 4b). Resulting parameter values at 0.95 confidence level are $v_p = (332 \pm 4)$ mm/s, $x' = (57.7 \pm 0.5)$ mm and $D = (2.8 \pm 0.9) \times 10^{-5}$ m^2/s. The values are reasonable: Flow velocity v_p is only slightly above the value measured by TOF RD MRI experiment (300 mm/s) [23], detector location x' is the same as the measured value within the experimental accuracy and, according to the Chapman-Enskog theory [40], diffusion coefficient of pure propane gas is 0.6×10^{-5} m^2/s, but in the gas mixture it is larger, as was observed. Hence, the results show also that RD travel time experiment could be used even as an alternative NMR method that does not require magnetic field gradients for determining self-diffusion coefficient of fluids. The increase of the measured diffusion coefficient caused by Taylor dispersion is insignificant, only about 1.6%.

3.2. Poiseuille-like flow in a capillary

Original travel time experiment was carried out for water flowing in the capillary, and resulting travel time distribution obtained by substituting the measured travel time curve amplitudes to Eq. (7) is shown in Fig. 5. The shape of the water travel time distribution indicates Poiseuille-like flow (compare with Fig. 1c). This is reasonable, because the Reynolds number was estimated to be small, about 25, implying that the flow is laminar, and the average diffusion time of water ($D = 2 \times 10^{-9}$ m^2/s [37]) across the capillary (about 6 s) is now longer than the travel time (on the order of 200 ms), preventing complete mixing of flow lamellas. The distribution has its maximum value at $t = 180$ ms, indicating that the maximum flow velocity is $v_{lmax} = x'/t = 58$ mm/180 ms = 320 mm/s. The average flow velocity, which is a half of the maximum flow velocity, measured by TOF RD MRI experiments is about 170 mm/s [23], indicating that the maximum velocity is slightly larger, about

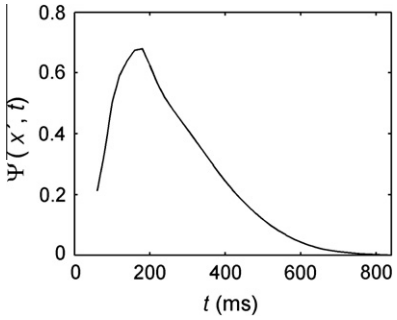

Fig. 5. Travel time distribution of water flowing in the capillary measured using the original travel time pulse sequence. Time resolution in the experiment was 20 ms and number of consecutive FID signals collected during one scan was 40.

340 mm/s. The slightly smaller value deduced from the travel time distribution may be a consequence of partial mixing of flow lamellas (see below).

A closer comparison of Figs. 5 and 1c reveals that measured and model travel time distribution deviate slightly from each other because of several reasons. Firstly, the maximum velocity in the experiment was slightly larger (340 mm/s) than in the model (300 mm/s), shifting the maximum of the distribution toward smaller travel times. Secondly, mixing of the flow lamellas during travel time is actually quite significant due to transverse diffusion: For example, the average diffusion distance in 500 ms is about 45 μm, which is almost one third of the radius of the capillary. As a consequence of the mixing of the flow lamellas, the maximum of the measured distribution is larger and the distribution approaches zero faster at larger t values than in the model distribution. Because of T_1 relaxation, the distribution is also weighted by the exponential factor shown in Eq. (13). Other, less significant factors deviating the shape of the measured distribution from that of the model distribution are imperfect excitation profile of the encoding coil, axial diffusion and stretching and folding of the liquid in the bend of the tubing [41].

3.3. Gas flow in microfluidic chips

In the next experiment, hyperpolarized propane gas flowed through Chip 1 containing an enlargement section between two narrow channel sections (see Fig. 6a). The travel time distribution measured by the original experiment is shown in Fig. 7a. The distribution can be thought to be comprised of three peaks, whose maxima are at $t \sim 70$, 135 and 200 ms. Without any dispersion of the gas molecules, the distribution would be rectangular as the propagator for plug flow is the Dirac delta function, and the maximum value of the distribution would be one. Consequently, the distribution profile shows that the dispersion of the molecules is significant. Probably, the dispersion is largest in the inlet and outlet connectors, as RD MRI experiments performed with hyperpolarized xenon flowing in a similar chip implies that the connectors comprise two volumes from which one is effectively connected to the flow field and the other gets exchanged only slowly [20]. By comparing the travel time distribution and RD MRI result [23], the first peak can be associated with the molecules inside the large volume of the outlet connector, the second peak with the molecules in the channels of the chip, and the third peak inside the inlet connector volume during the encoding. The dips between the peaks are likely caused by imperfect inversion of the spins due to magnetic field inhomogeneity in the interface between the inlet/outlet connector and flow channel.

The travel time distribution of propane gas flowing through Chip 2 containing ladder-like channel structure is shown in Fig. 7b. As in the case of Chip 1, the travel time distribution can

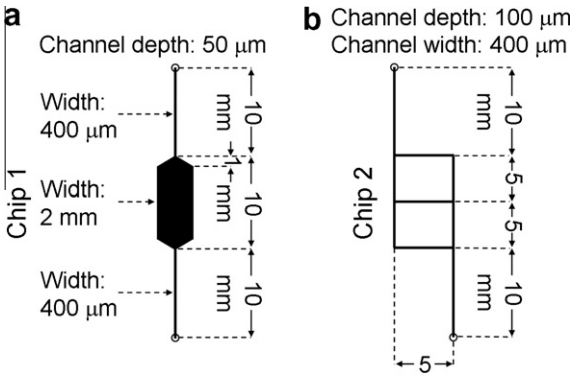

Fig. 6. Channel geometry of Chip 1 (a) and Chip 2 (b). According to the manufacturer (Translume, Inc., Ann Arbor, Michigan), the tolerance of the channel dimensions is ±20 μm. The chips were made of fused silica, and the height, width and thickness of the chip plates were 40, 15 and 1 mm, respectively. The channels were connected to the inlet and outlet capillaries by Nanoport connectors glued on the top of the hole from the channel to surface of the chip indicated by circles in the figure. Other details of the flow setup are described elsewhere [23].

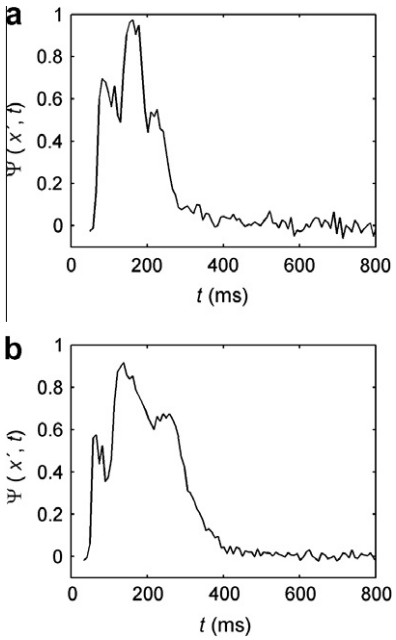

Fig. 7. Travel time curve of hyperpolarized propane flowing in (a) Chip 1 and (b) Chip 2 measured by the original travel time experiment. Time resolution in the experiments was 8 ms. Number of consecutive FID signals collected during one scan was 100.

be considered to be comprised of three different peaks, whose tops are at $t \sim 65$, 140 and 250 ms, and these can be associated with the molecules originally in the inlet connector volume, chip channels and outlet connector volume, respectively. The distribution profile indicates that the dispersion of the molecules is significant also in this case. Total travel time through Chip 2 is larger than in the case of Chip 1, as the total channel volume in Chip 2 is about 1.7 times larger that in Chip 1.

3.4. Comparison between the original and modified travel time experiments

The travel time curve of hyperpolarized propane flowing in the capillary measured using the modified pulse sequence is shown in Fig. 8a. As indicated in Eq. (8), the curve is directly the travel time distribution. Comparison between Figs. 8a and 4b confirms that the

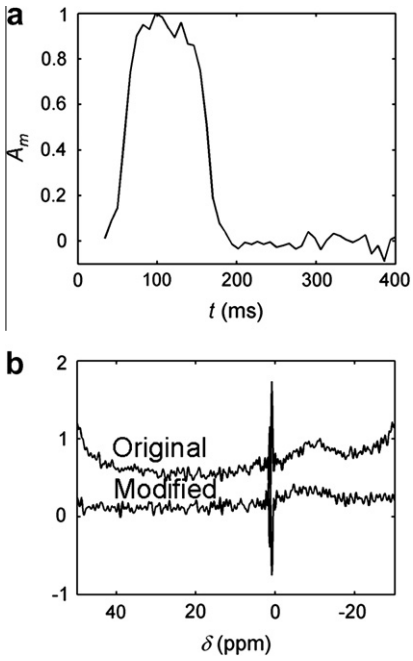

Fig. 8. (a) Travel time curve of hyperpolarized propane flowing in the capillary measured by the modified experiment. Time resolution and number of consecutive FID signals collected during one scan were the same as in the original travel time experiment shown in Fig. 4a. (b) The spectra measured at t = 114 ms, corresponding to the minimum amplitude (*i.e.*, maximum negative amplitude) in the original experiment and maximum amplitude in the modified experiment.

shape of the travel time distributions given by the original and modified experiments is the same. Fitting of the model function to the experimental data points resulted in almost equal values of the parameters v_p, x' and D as in the case of the original experiment (see Section 3.1); the differences were below 1%.

The spectra measured at the same travel time instance in the original and modified experiment are seen in Fig. 8b. The baseline of the spectra in the original experiment is distorted and its average level is much above the zero level. This is a consequence of the background signal arising from the protons in the capillary walls. The distortions in the spectrum of the modified experiment are significantly smaller, demonstrating the ability of the modified experiment to remove undesired background signals. However, the suppression is not perfect, because the baseline level is slightly above the zero level. Possibly, the relaxation time of the background signal is so short that it is comparable with the pulse length, and this causes the imperfect suppression. The absolute noise level in the travel time curves shown in Figs. 8a and 4a is the same. However, the signal amplitude varies between −1 and 1 in the original experiment whereas the scale is from 0 to 1 in the modified experiment, and therefore, effectively, the noise level is double in the travel time distribution given by the modified travel time experiment, as can be seen by comparing Figs. 8a and 4b. Hence, we summary that, on one hand, the modified travel time experiment suppresses the signal of the unencoded spins and the background signal and it reveals directly the travel time distribution without inversion, but, on the other hand, it effectively decreases the signal-to-noise ratio in the travel time distribution by factor of two. Hence, the modified experiment is more practical when the signal-to-noise ratio in the experiment is good enough.

4. Conclusions

Appearance of Poiseuille and plug flow in the remote detection travel time curves measured from a fluid flowing in a capillary was analyzed in detail. Experimental demonstrations showed that water flow in the capillary corresponds to the Poiseuille-like flow whereas gas flow in the capillary is manifested as plug-like flow because of fast diffusional mixing. Quantitative analysis of gas flow requires taking into account the axial diffusion of gas and imperfect excitation profile of the encoding coil. In the case of water flow, another important factor is transverse diffusion which partially mixes successive flow lamellas. We interpreted also how geometry of the flow channels is reflected in the travel time distributions measured from microfluidic devices. In addition, modified travel time experiment, which removes the signal of the unencoded probe fluid spins as well as the background signal arising from the material inside or close to the detector, was introduced and applied.

Acknowledgments

This work was funded by the grants from the Academy of Finland (123847, 132132 and 139839), University of Oulu, RAS (5.1.1), SB RAS (67, 88), the program of support of leading scientific schools (NSh-7643.2010.3) and FASI (State Contract 02.740.11.0262). Authors are grateful to professors J. Jokisaari and I. V. Koptyug for helpful discussions and comments.

References

[1] G.M. Whitesides, The origins and the future of microfluidics, Nature 446 (2006) 368–373.
[2] M.A. Burns, B.N. Johnson, S.N. Brahmasandra, K. Handique, J.R. Webster, M. Krishn, An integrated nanoliter DNA analysis device, Science 282 (1998) 484–487.
[3] C.L. Hansen, E. Skordalakes, J.M. Berger, S.R. Quake, A robust and scalable microfluidic metering method that allows protein crystal growth by free interface diffusion, Proc. Natl. Acad. Sci. USA 99 (2002) 16531–16536.
[4] A.R. Wheeler, W.R. Throndset, R.J. Whelan, A.M. Leach, R.N. Zare, Y.H. Liao, K. Farrell, I.D. Manger, A. Daridon, Microfluidic device for single-cell analysis, Anal. Chem. 75 (2003) 3581–3586.
[5] P.T. Callaghan, Principles of Nuclear Magnetic Resonance Microscopy, Clarendon Press, Oxford, 1991.
[6] E. Harel, Magnetic resonance detection: spectroscopy and imaging of lab-on-a-chip, Lab. Chip 9 (2009) 17–23.
[7] C. Massin, F. Vincent, A. Homsy, K. Ehrmann, G. Boero, P.A. Besse, A. Daridon, E. Verpoorte, N.F. de Rooij, R.S. Popovic, Planar microcoil-based microfluidic NMR probes, J. Magn. Reson. 164 (2003) 242–255.
[8] H. Wensink, F. Benito-Lopez, D.C. Hermes, W. Verboom, H.J. Gardeniers, D.N. Reinhoudt, A. van den Berg, Measuring reaction kinetics in a lab-on-a-chip by microcoil NMR, Lab. Chip 5 (2005) 280–284.
[9] J.D. Trumbull, I.K. Glasgow, D.J. Beebe, R.L. Magin, Integrating microfabricated fluidic systems and NMR spectroscopy, IEEE Trans. Biomed. Eng. 47 (2000) 3–7.
[10] S. Ahola, F. Casanova, J. Perlo, K. Münnemann, B. Blümich, S. Stapf, Monitoring of fluid motion in a micromixer by dynamic NMR microscopy, Lab. Chip 6 (2006) 90–95.
[11] A.J. Moule, M. Spence, S. Han, J. Seeley, K. Pierce, S. Saxena, A. Pines, Amplification of xenon NMR and MRI by remote detection, Proc. Natl. Acad. Sci. USA 100 (2003) 9122–9127.
[12] S. Xu, V.V. Yashchuk, M.H. Donaldson, S.M. Rochester, D. Budker, A. Pines, Magnetic resonance imaging with an optical atomic magnetometer, Proc. Natl. Acad. Sci. USA 103 (2006) 12668–12671.
[13] F. Verpillat, M.P. Ledbetter, D. Budker, S. Xu, D. Michalak, C. Hilty, L.-S. Bouchard, S. Antonijevic, A. Pines, Remote detection of nuclear magnetic resonance with an anisotropic magnetoresistive sensor, Proc. Natl. Acad. Sci. USA 105 (2008) 2271–2273.
[14] M. Ledbetter, I.M. Savukov, D. Budker, V. Shah, S. Knappe, J. Kitching, D.J. Michalak, S. Xu, A. Pines, Zero-field remote detection of NMR with a microfabricated atomic magnetometer, Proc. Natl. Acad. Sci. USA 105 (2008) 2286–2290.
[15] J. Granwehr, E. Harel, S. Han, S. Garcia, A. Pines, Time-of-flight flow imaging using NMR remote detection, Phys. Rev. Lett. 95 (2005) 075503.
[16] J.A. Seeley, S.-I. Han, A. Pines, Remotely detected high-field MRI of porous samples, J. Magn. Reson. 167 (2004) 282–290.
[17] E. Harel, J. Granwehr, J. Seeley, A. Pines, Multiphase imaging of gas flow in a nanoporous material using remote-detection NMR, Nat. Mater. 5 (2006) 321–327.
[18] V.-V. Telkki, C. Hilty, S. Garcia, E. Harel, A. Pines, Quantifying the diffusion of a fluid through membranes by double phase encoded remote detection magnetic resonance imaging, J. Phys. Chem. B 111 (2007) 13929–13936.
[19] E.E. McDonnell, S. Han, C. Hilty, K.L. Pierce, A. Pines, NMR analysis on microfluidic devices by remote detection, Anal. Chem. 77 (2005) 8109–8114.

[20] C. Hilty, E. McDonnell, J. Granwehr, K. Pierce, S. Han, A. Pines, Microfluidic gas-flow profiling using remote-detection NMR, Proc. Natl. Acad. Sci. USA 102 (2005) 14960–14963.
[21] E. Harel, C. Hilty, K. Koen, E.E. McDonnell, A. Pines, Time-of-flight flow imaging of two-component flow inside a microfluidic chip, Phys. Rev. Lett. 98 (2007) 017601.
[22] E. Harel, A. Pines, Spectrally resolved flow imaging of fluids inside a microfluidic chip with ultrahigh time resolution, J. Magn. Reson. 193 (2008) 199–206.
[23] V.-V. Telkki, V.V. Zhivonitko, S. Ahola, K.V. Kovtunov, J. Jokisaari, I.V. Koptyug, Microfluidic gas flow imaging utilizing parahydrogen-induced polarization and remote detection NMR, Angew. Chem. Int. Ed. 49 (2010) 8363–8366.
[24] V.-V. Telkki, J. Saunavaara, J. Jokisaari, Time-of-flight remote detection MRI of thermally modified wood, J. Magn. Reson. 202 (2010) 78–84.
[25] M.S. Anwar, C. Hilty, C. Chu, L.-S. Bouchard, K.L. Pierce, A. Pines, Spin coherence transfer in chemical transformations monitored by remote detection NMR, Anal. Chem. 79 (2007) 2806–2811.
[26] Z.I. Cleveland, G.E. Pavlovskaya, K.F. Stupic, C.F. LeNoir, T. Meersmann, Exploring hyperpolarized ^{83}Kr by remotely detected NMR relaxometry, J. Chem. Phys. 124 (2006) 044312.
[27] X. Zhou, D. Graziani, A. Pines, Hyperpolarized xenon NMR and MRI signal amplification by gas extraction, Proc. Natl. Acad. Sci. USA 106 (2009) 16903–16906.
[28] C.R. Bowers, D.P. Weitekamp, Transformation of symmetrization order to nuclear-spin magnetization by chemical reaction and nuclear magnetic resonance, Phys. Rev. Lett. 57 (1986) 2645–2648.
[29] C.R. Bowers, D.P. Weitekamp, Parahydrogen and synthesis allow dramatically enhanced nuclear alignment, J. Am. Chem. Soc. 109 (1987) 5541–5542.
[30] I.V. Koptyug, K.V. Kovtunov, S.R. Burt, M.S. Anwar, C. Hilty, S.-I. Han, A. Pines, R.Z. Sagdeev, Para-hydrogen-induced polarization in heterogeneous hydrogenation reactions, J. Am. Chem. Soc. 129 (2007) 5580–5586.
[31] L.-S. Bouchard, K.V. Kovtunov, S.R. Burt, M.S. Anwar, I.V. Koptyug, R.Z. Sagdeev, A. Pines, Para-hydrogen-enhanced hyperpolarized gas-phase magnetic resonance imaging, Angew. Chem. Int. Ed. 46 (2007) 4064–4068.
[32] L.S. Bouchard, S.R. Burt, M.S. Anwar, K.V. Kovtunov, I.V. Koptyug, A. Pines, NMR imaging of catalytic hydrogenation in microreactors with the use of para-hydrogen, Science 319 (2008) 442–445.
[33] K.V. Kovtunov, I.E. Beck, V.I. Bukhtiyarov, I.V. Koptyug, Observation of parahydrogen-induced polarization in heterogeneous hydrogenation on supported metal catalysts, Angew. Chem. Int. Ed. 47 (2008) 1492–1495.
[34] S.-I. Han, B. Blümich, Two-dimensional representation of position, velocity and acceleration by PFG-NMR, Appl. Magn. Reson. 18 (2000) 101–114.
[35] S.-I. Han, S. Stapf, B. Blümich, Two-dimensional PFG NMR for encoding correlations of position, velocity, and acceleration in fluid transport, J. Magn. Reson. 146 (2000) 169–180.
[36] M.G. Pravica, D.P. Weitekamp, Net NMR alignment by adiabatic transport of para-hydrogen addition-products to high magnetic-field, Chem. Phys. Lett. 145 (1988) 255–258.
[37] P. Kekkonen, V.-V. Telkki, J. Jokisaari, Determining the highly anisotopic cell structures of Pinus Sylvestris in three orthogonal directions by PGSTE NMR of absorbed water and methane, J. Phys. Chem. B 113 (2009) 1080–1084.
[38] G. Taylor, Dispersion of soluble matter in solvent flowing slowly through a tube, Proc. Roy. Soc. A 219 (1953) 186–203.
[39] D.I. Hoult, R.E. Richards, The signal-to-noise ratio of the nuclear magnetic resonance experiment, J. Magn. Reson. 24 (1976) 71–85.
[40] E.L. Cussler, Diffusion: Mass Transfer in Fluid Systems, Cambridge University Press, Cambridge, 1997.
[41] M.R. Bringer, C.J. Gerdts, H. Song, J.D. Tice, R.F. Ismagilov, Microfluidic systems for chemical kinetics that rely on chaotic mixing in droplets, Philos. Trans. Roy. Soc. Lond. A 362 (2004) 1087–1104.